

Implications of the search for optical counterparts during the first six months of the Advanced LIGO's and Advanced Virgo's third observing run: possible limits on the ejecta mass and binary properties

Michael W. Coughlin¹,¹★ Tim Dietrich,² Sarah Antier³,³ Mattia Bulla^{4,5},^{4,5} Francois Foucart,⁶ Kenta Hotokezaka,⁷ Geert Raaijmakers,⁸ Tanja Hinderer⁸ and Samaya Nissanke^{8,9}

¹California Institute of Technology, 1200 East California Blvd, MC 249-17, Pasadena, CA 91125, USA

²Nikhef, Science Park, NL-1098 XG Amsterdam, the Netherlands

³APC, UMR 7164, 10 rue Alice Domon et Léonie Duquet, F-75205 Paris, France

⁴Nordita, KTH Royal Institute of Technology and Stockholm University, Roslagstullsbacken 23, SE-106 91 Stockholm, Sweden

⁵Oskar Klein Centre, Department of Physics, Stockholm University, SE-106 91 Stockholm, Sweden

⁶Department of Physics & Astronomy, University of New Hampshire, 9 Library Way, Durham NH 03824, USA

⁷Department of Astrophysical Sciences, Princeton University, Princeton, NJ 08544, USA

⁸GRAPPA, Anton Pannekoek Institute for Astronomy and Institute of High-Energy Physics, University of Amsterdam, Science Park 904, NL-1098 XH Amsterdam, the Netherlands

⁹Nikhef, Science Park 105, NL-1098 XG Amsterdam, the Netherlands

Accepted 2019 December 5. Received 2019 December 4; in original form 2019 October 24

ABSTRACT

GW170817 showed that neutron star mergers not only emit gravitational waves but also can release electromagnetic signatures in multiple wavelengths. Within the first half of the third observing run of the Advanced LIGO and Virgo detectors, there have been a number of gravitational wave candidates of compact binary systems for which at least one component is potentially a neutron star. In this article, we look at the candidates S190425z, S190426c, S190510g, S190901ap, and S190910h, predicted to have potentially a non-zero remnant mass, in more detail. All these triggers have been followed up with extensive campaigns by the astronomical community doing electromagnetic searches for their optical counterparts; however, according to the released classification, there is a high probability that some of these events might not be of extraterrestrial origin. Assuming that the triggers are caused by a compact binary coalescence and that the individual source locations have been covered during the EM follow-up campaigns, we employ three different kilonova models and apply them to derive possible constraints on the matter ejection consistent with the publicly available gravitational-wave trigger information and the lack of a kilonova detection. These upper bounds on the ejecta mass can be related to limits on the maximum mass of the binary neutron star candidate S190425z and to constraints on the mass-ratio, spin, and NS compactness for the potential black hole–neutron star candidate S190426c. Our results show that deeper electromagnetic observations for future gravitational wave events near the horizon limit of the advanced detectors are essential.

Key words: gravitational waves – methods: statistical.

1 INTRODUCTION

By the combined detection of GW170817, AT2017gfo, and GRB170817A, the field of multimessenger astronomy was ushered into a new era in which gravitational-wave (GW) and electromag-

netic (EM) signatures are simultaneously measured and analysed (e.g. Tanvir et al. 2013; Abbott et al. 2017, 2017b; Arcavi et al. 2017; Coulter et al. 2017; Lipunov et al. 2017; Mooley et al. 2017; Savchenko et al. 2017; Soares-Santos et al. 2017; Troja et al. 2017; Valenti et al. 2017). Joint analyses allow a better understanding of the supranuclear-dense matter inside neutron stars (NSs; e.g. Radice et al. 2018; Bauswein et al. 2017; Margalit & Metzger 2017; Coughlin et al. 2018, 2019b; Rezzolla, Most & Weih 2018; Capano

★ E-mail: mcoughli@caltech.edu

et al. 2019; Radice & Dai 2019), a precise measurement of the speed of gravitational waves (Abbott et al. 2017c), an independent measurement of the expansion rate of the Universe (Abbott et al. 2017a; Hotokezaka et al. 2019; Coughlin et al. 2019a; Dhawan et al. 2019), and constraints on alternative models of gravity (Baker et al. 2017; Creminelli & Vernizzi 2017; Ezquiaga & Zumalacárregui 2017; Sakstein & Jain 2017).

In general, the merger of two compact objects from which at least one is a NS, is connected to a variety of possible EM signatures in almost all wavelengths. A highly relativistic jet can produce a short gamma-ray burst (sGRB) lasting a few seconds (Eichler et al. 1989; Paczynski 1991; Narayan, Paczynski & Piran 1992; Mochkovitch et al. 1993; Lee & Ramirez-Ruiz 2007; Nakar 2007) and a synchrotron afterglow in the X-rays, optical and radio visible bands for hours to months after the initial emission due to the deceleration of the jet into the ambient media (Sari, Piran & Narayan 1998). The ejection of highly neutron-rich material, being the seed of r-process elements (Lattimer & Schramm 1974, 1976), powers a thermal ultraviolet/optical/near-infrared kilonova due to the radioactive decay of the new heavy elements produced in the ejecta (Li & Paczynski 1998; Metzger et al. 2010; Roberts et al. 2011; Kasen et al. 2017). Although the colour and luminosity of a kilonova will be viewing angle dependent, the kilonova signature is, in contrast to the sGRB and its afterglow, likely visible from all viewing angles. This means that after every merger which ejects a sufficient amount of material, one should be able to observe a kilonova regardless of the orientation of the system (Roberts et al. 2011). Thus, kilonovae provide a *smoking guns* evidence for binary neutron star (BNS) and black hole–neutron star (BHNS) mergers.

However, current numerical relativity studies indicate that not all BNS or BHNS collisions will eject enough material to create EM signals as bright as the one observed for GW170817. For most BNS systems, the EM signals are expected to be dimmer than for GW170817 if a black hole (BH) forms directly after the moment of merger, since for these *prompt collapse* configurations the amount of ejected material and the mass of the potential debris disc is expected to be very small. Whether a merger remnant undergoes a prompt collapse depends mostly on its total mass (Bauswein, Baumgarte & Janka 2013; Hotokezaka et al. 2013; Dietrich & Ujevic 2017; Agathos et al. 2019; Köppel, Bovard & Rezzolla 2019) but also seems to be sub-dominantly affected by the mass ratio (Kiuchi et al. 2019). For highly asymmetric mass ratios ($m_1/m_2 \lesssim 0.8$), there could be a non-negligible ejecta mass and/or a massive accretion disc around the BH remnant even for prompt collapse scenarios (Kiuchi et al. 2019).

In the case of a BHNS system, the brightness of the potential EM counterpart depends on whether the NS gets tidally disrupted by the BH and, thus, ejects a large amount of material and forms a massive accretion disc; or if the star falls into the BH without disruption, preventing the production of GRBs and kilonovae. Thus, the outcome of the merger is mostly determined by the mass ratio of the binary, the spin of the BH, and the compactness of the NS, with disruption being favoured for low-mass, rapidly rotating BH and large NS radii (Etienne et al. 2009; Pannarale, Tonita & Rezzolla 2011; Foucart 2012; Kyutoku et al. 2015; Kawaguchi et al. 2016; Foucart, Hinderer & Nissanke 2018).

Since the beginning of the third observation run, a number of potential GW events have triggered extensive follow-up campaigns to search for possible EM counterparts, most notably S190425z (LIGO Scientific Collaboration & Virgo Collaboration 2019a, b), S190426c (LIGO Scientific Collaboration & Virgo Collaboration 2019c, s), S190510g (LIGO Scientific

Table 1. Overview about officially non-retracted GW triggers with large probabilities to be BNS or BHNS systems. The individual columns refer to: the name of the event, an estimate using the most up-to-date classification for the event to be a BNS [p(BNS)], a BHNS [p(BHNS)], or terrestrial noise [p(terrestrial)] (Kapadia et al. 2019), and an indicator to estimate the probability of producing EM signature considering the candidate with astrophysical origin [p(HasRemnant)], whose definition is in the LIGO–Virgo alert userguide. Note that the alert can be also classified as ‘MassGap’, completing the possible classifications. Note that within our analysis, we do not consider S190718y because of its very low probability to be of astrophysical origin.

Name	p(BNS) (per cent)	p(BHNS) (per cent)	p(terr.) (per cent)	p(HasRemn.) (per cent)
S190425z	> 99	0	< 1	> 99
S190426c	24	6	58	> 99
S190510g	42	0	58	> 99
S190718y*	2	0	98	> 99
S190814bv	0	> 99	< 1	< 1
S190901ap	86	0	14	> 99
S190910d	0	98	2	< 1
S190910h	61	0	39	> 99
S190923y	0	68	32	< 1
S190930t	0	74	26	< 1

Collaboration & Virgo Collaboration 2019f), S190814bv (LIGO Scientific Collaboration & Virgo Collaboration 2019o), S190901ap (LIGO Scientific Collaboration & Virgo Collaboration 2019t), S190910h (LIGO Scientific Collaboration & Virgo Collaboration 2019w), S190910d (LIGO Scientific Collaboration & Virgo Collaboration 2019v), S190923y (LIGO Scientific Collaboration & Virgo Collaboration 2019z), and S190930t (LIGO–Virgo collaboration 2019; cf. Table 1 for more details).¹ The large size of localization regions with thousands of square degrees have proved much more challenging to cover over short times than the ~ 20 deg² of GW170817. In fact, no joint detection of GW and EM signals has been confirmed; see also Dado & Dar (2019) for a possible explanation that no sGRBs has been observed for the GW events within O3a. While a detection of an EM signature will help significantly to unravel some of the remaining open questions related to compact binary mergers, the possibility of a ‘missing’ EM signature for an astrophysical relevant trigger whose sky location was covered during an EM follow-up campaign also delivers some information about the source properties, as we will discuss.

¹ Additional alerts have been sent out for other triggers, but those have been retracted. A BNS candidate S190718y (LIGO Scientific Collaboration & Virgo Collaboration 2019k) was sent to the astronomical community; due to the presence of a strong glitch near to the trigger time, only a few optical observations were performed and this alert will not be considered in this study. In addition, other candidates S190518bb (LIGO Scientific Collaboration & Virgo Collaboration 2019i), S190524q (LIGO Scientific Collaboration & Virgo Collaboration 2019j), S190808ae (LIGO Scientific Collaboration & Virgo Collaboration 2019n), S190816i (LIGO Scientific Collaboration & Virgo Collaboration 2019q), and S190822c (LIGO Scientific Collaboration & Virgo Collaboration 2019r) were also identified and later retracted. In addition, an interesting BH merger candidate triggered intensive follow-up due to its low latency properties results with the possibility to have one object between 3 and 5 solar mass (LIGO Scientific Collaboration & Virgo Collaboration 2019l), but updated results with the full exploration of the parameter space of masses and spins, finally did not confirm these properties (LIGO Scientific Collaboration & Virgo Collaboration 2019m).

In this article, we try to understand if from the detection or, more likely, non-detection of an EM counterpart to a potential GW event it is possible to place constraints on the merger outcome and the properties of the system. For this purpose, we will shortly summarize the EM follow-up campaigns of S190425z, S190426c, S190510g, S190814bv, S190901ap, S190910d, S190910h, S190923y, and S190930t in Section 2. We further also refer to Andreoni et al. (2019a) for a dedicated discussion done by the GROWTH collaboration about S190814bv.

In Section 3, we focus on the events for which the `HasRemnant`² prediction provides a high probability of a potential EM signature (S190425z, S190426c, S190510g, S190901ap, and S190910h;³ cf. Table 1). Under the assumption that the GW candidate location was covered during the EM observations, we will use a set of three different light-curve models (Kasen et al. 2017; Bulla 2019; Hotokezaka & Nakar 2019) to predict the properties of the kilonova consistent with the non-observation of an EM counterpart. This analysis allows us to derive constraints on the maximum ejecta mass for each event in Section 3 and connects our findings to the binary properties in Section 4. These constraints are typically not very striking, given the large distance to the GW triggers in the first half of advanced LIGO and advanced Virgo’s third observing run, which highlights that, if possible, longer exposure times should be employed to reduce the possibility that interesting transients might be missed. We summarize our conclusions and lessons learned for observations in the second half of the third observing run in Section 5.

2 EM FOLLOW-UP CAMPAIGNS

We summarize the EM follow-up work of the various teams that performed synoptic coverage of the sky localization area and who have circulated their findings in publicly available circulars during the first six months of the third observing run. For a summary of the follow-up campaign during the second observing run, please see Abbott et al. (2019) and references therein. We differentiate the candidates by their classification (predominantly BNS in Table A1 and predominantly BHNS in Table A2). While this is mostly an initial classification and may change based on future offline estimates, we think it is useful as, for example, the distance estimates tend to be different between these classes. A short discussion about each candidate is presented below; note that we do not report the observations that exclusively target galaxies.

2.1 S190425z

LIGO/Virgo S190425z was identified by the LIGO Livingston Observatory (L1) and the Virgo Observatory (V1) at 2019-04-25 08:18:05.017 UTC (LIGO Scientific Collaboration & Virgo Collaboration 2019a, b). LIGO Hanford Observatory (H1) was not taking data at the time. It has been so far categorized as a BNS signal, reported as a BNS (99 per cent) with a small probability of being in the mass gap (< 1 per cent). Due to the low signal-to-noise ratio (SNR) in V1, S190425z’s sky localization is relatively poor,

²<https://emfollow.docs.ligo.org/userguide/content.html> and <https://dcc.ligo.org/LIGO-P1900291>. Typically, the `HasRemnant` classification employs the disc mass estimate of Foucart et al. (2018) and applies to BHNS systems. BNS configurations are assumed to cause an EM signature, which, as we show later, might not be correct. The `HasRemnant` classification assumes the event to be of astrophysical origin and does not incorporate the possibility that the trigger is caused by noise.

³We do not include S190718y because of its high probability to be noise.

covering nearly $10\,000\text{ deg}^2$. The original distance quoted for this system is $155 \pm 45\text{ Mpc}$, thus, about ~ 4 times further away than GW170817.

As the first alert during the O3 campaign with a high probability of having a counterpart, there was an intense follow-up campaign within the first $\sim 72\text{ h}$ after the initial notice (see ≈ 120 reports in GCN archive, mostly focusing on optical follow-up). As expressed in Cook et al. (2019), with more than 50 000 galaxies compatible with the 90 per cent sky area volume due to the large uncertainty of the localization, it was difficult to fully cover S190425z’s localization. However, as shown in Table A1, 10 telescopes reported tiling observations of the localization. For example, both the Zwicky Transient Facility (ZTF; Bellm et al. 2018; Masci et al. 2018; Dekany et al. 2019; Graham et al. 2019), a camera and associated observing system on the Palomar 48 inch telescope, and Palomar Gattini-IR, a new wide-field near-infrared survey telescope at Palomar observatory, followed up S190425c extensively (Coughlin et al. 2019c). Covering about 8000 and 2200 deg^2 , respectively, the systems achieved depths of $\approx 21\text{ mag}$ in g and r bands with ZTF and 15.5 mag in J band with Gattini-IR. Among them, using the LAL-Inference skymap, about 21 per cent of and 19 per cent of the sky localization was covered by ZTF and Palomar Gattini-IR, respectively. In addition, Pan-STARRS covered 28 per cent of the bayestar sky localization area in g -band with a limiting magnitude of $i = 21.5\text{ mag}$ (Smith et al. 2019); similarly, GOTO covered 30 per cent of the initial skymap down to $L = 20.5\text{ mag}$ (Steeghs et al. 2019a).

2.2 S190426c

LIGO/Virgo S190426c was identified by H1, L1, and V1 at 2019-04-26 15 : 21 : 55.337 UTC (LIGO Scientific Collaboration & Virgo Collaboration 2019c, s). With a probability of 58 per cent to be terrestrial, S190426c might not be of astrophysical origin. But assuming that the signal is of astrophysical relevance, S190426c seems to be a BHNS system with relative probabilities of approximately $12 : 5 : 3 : 0$ for the categories NSBH : MassGap : BNS : BBH, respectively (LIGO Scientific Collaboration & Virgo Collaboration 2019e). Within this analysis, the `HasRemnant` probability is stated as 72 per cent, thus, for all events with large `HasRemnant` predictions, is our best example for a possible BHNS merger. S190426c’s sky localization, given that it was discovered by multiple interferometers, covers less area than S190425z. The initial 90 per cent credible region was 1260 deg^2 with a luminosity distance of $375 \pm 108\text{ Mpc}$ (LIGO Scientific Collaboration & Virgo Collaboration 2019c). The updated skymap, sent 48 h after the initial skymap, had a 90 per cent credible region of 1130 deg^2 and a luminosity distance estimate of $377 \pm 100\text{ Mpc}$ (LIGO Scientific Collaboration & Virgo Collaboration 2019d). As the first event announced with a significant probability of a BHNS nature, the interest in this event was large and about 70 circulars have been sent out (see the GCN archive). As shown in Table A2, 13 telescopes scanned the localization region; for example, ASAS-SN (Shappee et al. 2019), GOTO (Steeghs et al. 2019b), and ZTF (Kasliwal et al. 2019b) covered more than 50 per cent of the sky localization area using multiple filters in the first 48 h.

2.3 S190510g

LIGO/Virgo S190510g was identified by H1, L1, and V1 at 2019-05-10 02 : 59 : 39.292 UTC (LIGO Scientific Collaboration & Virgo Collaboration 2019f). S190510g’s latest sky localization covers 1166 deg^2 with a luminosity distance of $227 \pm 92\text{ Mpc}$ (LIGO

Scientific Collaboration & Virgo Collaboration 2019g). In the most recent update provided by the LIGO and Virgo Collaboration, the event is now more likely caused by noise (LIGO Scientific Collaboration & Virgo Collaboration 2019h) than it is to be an astrophysical source, with a probability of terrestrial (58 per cent) and BNS (42 per cent); however, since the event is, up to now, not officially retracted, we will consider it in this article. Due to its potential BNS nature and its trigger time being close to the beginning of the night in the Americas, the event was followed-up rapidly, with about 60 circulars produced (see GCN archive). With ~ 65 per cent coverage of the LALInference skymap, GROWTH-DECam realized the deepest follow-up (Andreoni et al. 2019b). We can compute the joint coverage of different telescopes based upon their pointings and field of view reporting in the GCNs. Within 24 h, CNEST, HMT, MASTER, Xinglong, and TAROT, all with clear filters down to 18 mag, observed 71 per cent of the LALInference sky localization area; this number would assuredly be higher with a coordinated effort.

2.4 S190814bv

The candidate S190814bv was identified by H1, L1, and V1 on 2019-08-14 21:10:39.013 UTC. First classified as a compact merger with one component having an initial mass between 3 and 5 solar masses (LIGO Scientific Collaboration & Virgo Collaboration 2019o), the candidate is now classified as a BHNS with posterior support from parameter estimation (Veitch et al. 2015) with NSBH (>99 per cent) (LIGO Scientific Collaboration & Virgo Collaboration 2019p). Initially, two different Bayestar-based sky localizations were generated, one with the lower false alarm rate which included Livingston and Virgo data (sent 21 min after the trigger time) and one with contribution of the three instruments (sent 2 h after the GW trigger time). A third skymap (LALInference) with all three interferometers was sent ~ 13.5 h after the trigger time. The initial three interferometer 90 per cent credible region was 38 deg^2 with a luminosity distance estimated at 276 ± 56 Mpc. The latest 90 per cent credible region is 23 deg^2 with a luminosity distance of 267 ± 52 Mpc. With the small localization region, and its location in the Southern hemisphere, the event was ideal for follow-up. However, no counterpart candidates remain after the extensive follow-up, with about 70 circulars produced (see GCN archive). As shown in Table A2, many survey systems covered a vast majority of the localization region, including ATLAS (Srivastav et al. 2019), DESGW-DECam (Soares-Santos et al. 2019), and TAROT (Klotz et al. 2019). We note here despite the small sky area and the intensive followed-up studies, we do not consider this object in the analysis due to its HasRemnant value. The joint coverage of MASTER and TAROT with 17 mag in clear filter within the first 3 h was about 90 per cent of the LALInference skymap.

2.5 S190901ap

LIGO/Virgo S190901ap was identified by L1 and V1 at 2019-09-01 23:31:01.838 UTC (LIGO Scientific Collaboration & Virgo Collaboration 2019t). The candidate is currently classified as BNS (86 per cent) and terrestrial (14 per cent). The latest 90 per cent credible region is $14\,753 \text{ deg}^2$ with a luminosity distance of 241 ± 79 Mpc (LIGO Scientific Collaboration & Virgo Collaboration 2019u), whereas the initial 90 per cent credible region was $13\,613 \text{ deg}^2$ with a luminosity distance of 242 ± 81 Mpc. Although considered as an interesting event due to a possible remnant, the large error box of thousands of square degrees led to a bit less interest in following-up the event (see ≈ 44 reports in GCN archive).

However, survey instruments such as GOTO (Ackley et al. 2019b), ZTF (Kool et al. 2019), and MASTER (Lipunov et al. 2019e) observed more than 30 per cent of the localization; in particular, ZTF covered more than 70 per cent.

2.6 S190910d

LIGO/Virgo S190910d was identified as a compact binary merger candidate by H1 and L1 at 2019-09-10 01:26:19.243 UTC (LIGO Scientific Collaboration & Virgo Collaboration 2019v). The candidate is currently classified as NSBH (98 per cent) and terrestrial (2 per cent). With an initial 90 per cent credible region of 3829 deg^2 with a luminosity distance of 606 ± 197 Mpc, the latest 90 per cent credible region is 2482 deg^2 with a luminosity distance of 632 ± 186 Mpc (LIGO Scientific Collaboration & Virgo Collaboration 2019x). Relatively few instruments participated in the follow-up of this object (see ≈ 25 reports in GCN archive). However, network instruments such as ZTF (Anand et al. 2019), GRANDMA-TAROT (Noysena et al. 2019), and MASTER (Lipunov et al. 2019f) observed 25 per cent of the skymap or more.

2.7 S190910h

LIGO/Virgo S190910h was identified as a compact binary merger candidate by only one detector (L1) at 2019-09-10 08:29:58.544 UTC (LIGO Scientific Collaboration & Virgo Collaboration 2019w). The candidate is currently classified as BNS (61 per cent) and terrestrial (39 per cent). The initial 90 per cent credible region was $24\,226 \text{ deg}^2$ with a luminosity distance of 241 ± 89 Mpc. The latest 90 per cent credible region is $24\,264 \text{ deg}^2$ with a luminosity distance of 230 ± 88 Mpc (LIGO Scientific Collaboration & Virgo Collaboration 2019y). Even fewer instruments participated in the follow-up of this object (see ≈ 20 reports in GCN archive) due to the previous alert (S190910d) that was just a few hours before, in addition to the very large localization. Only ZTF covered a significant portion of the localization (about 34 per cent in g/r band; Stein et al. 2019a).

2.8 S190923y

The candidate S190923y was identified by H1 and L1 at 2019-09-23 12:55:59.646 UTC. So far, only low-latency classification and sky localizations are publicly available (LIGO Scientific Collaboration & Virgo Collaboration 2019z). S190923y is classified with NSBH (>68 per cent) and Terrestrial (32 per cent) with low latency estimation. The bayestar initial sky localization area gives a 90 per cent credible region of 2107 deg^2 with a luminosity distance of 438 ± 133 Mpc. Due to the large uncertainty of the sky localization area and the distance luminosity above the completeness of most of the galaxy catalogues (see ≈ 17 reports in GCN archive), S190923y has been followed-up by surveys as GRANDMA-TAROT and MASTER in optical bands at ≈ 18 mag (Turpin et al. 2019; Lipunov et al. 2019h).

2.9 S190930t

The candidate was identified by L1 at 2019-09-30 14:34:07.685 UTC. So far, only low-latency classification and sky localizations are publicly available (LIGO-Virgo collaboration 2019). S190930t is classified with NSBH (74 per cent) and Terrestrial (26 per cent). The bayestar initial sky localization area gives a 90 per cent credible region of $24\,220 \text{ deg}^2$ with a luminosity distance of 108 ± 38 Mpc. A number of the survey instruments including ATLAS (Smartt

et al. 2019b), MASTER (Lipunov et al. 2019g), and ZTF Stein et al. (2019b) covered a significant portion of the localization above ≈ 19.5 mag.

2.10 Summary

There are a few takeaways from the above. The first is that dedicated robotic facilities, either in their generic survey mode or performing target of opportunity observations, are present throughout all events. Facilities such as TAROT, ZTF, and MASTER, all robotic survey instruments, contributed to kilonova searches for the vast majority of objects. However, we conducted calculation of joint coverage of the sky localization area for two different alerts S190510g and S190814bv with the three networks. The improvement in terms of time spent for exploring a large portion of the skymap is not huge due to the missing coordination of the individual groups. However, this approach might help in terms of having a certain location on the sky re-observed several times that potentially improves the constraints or detection prospects upon further data analysis. As can be seen from the table, other robotic survey systems also imaged portions of the localizations (for example, with their routine searches for near earth objects), but these serendipitous observations and associated new candidates were not always reported publicly. This may motivate use of the central reporting databases, if only to assess the level of coverage. In addition, one notices that, generally, the participation from other systems, at the candidate identification level at least, seemed to have dropped off as the semester went along.

3 MODELLING KILONOVA AND DERIVING POSSIBLE LIMITS FROM OBSERVATIONS

3.1 Kilonova modelling

We will employ three different kilonova models based on Kasen et al. (2017), Bulla (2019), and Hotokezaka & Nakar (2019), deriving constraints on possible kilonova light curves and their connected ejecta properties. With the use of multiple models, we hope to reduce systematic effects. For Models I and II, we employ a Gaussian process regression (GPR)-based interpolation (Doctor et al. 2017) to create a surrogate model for arbitrary ejecta properties (see Coughlin et al. 2018, 2019b for further details). The idea of this algorithm is to create interpolated, surrogate models for bolometric light curves, photometric light curves, or spectral energy distribution in sparse simulation sets typically provided by modelling software. For the photometric light curves, in particular, each passband is individually interpolated on to the same time array of 0.1 d and analysed separately. To support the interpolation, we perform a singular value decomposition (SVD) of a matrix composed of these light curves (separately for each passband); using this, we find eigenvalues and eigenvectors, which we will interpolate across the parameter space. To do so, we use the *sci-kit learn* (Pedregosa et al. 2011) implementation of GPR (Rasmussen & Williams 2006), which is a statistical interpolation method that produces a posterior distribution on a function f given known values of f at a few points in the parameter space. Model III is semi-analytic.

3.1.1 Model I (Kasen et al. 2017)

For the models presented in Kasen et al. (2017), each light curve depends on the ejecta mass M_{ej} , the mass fraction of lanthanides X_{lan} , and the ejecta velocity v_{ej} . To simplify the analysis, we use a one-component model that captures the broad features of AT2017gfo

as shown in Coughlin et al. (2017), in contrast to the use of a two-component model (Coughlin et al. 2018c) that improves the fit slightly but doubles the number of free parameters. We compute light curves consistent with the following prior choices: $-3 \leq \log_{10}(M_{\text{ej}}/M_{\odot}) \leq 0$, $0 \leq v_{\text{ej}} \leq 0.3c$. For the ejecta velocity, this covers the range used in the Kasen et al. (2017) simulation set; for the ejecta masses, where the simulation set covers $-3 \leq \log_{10}(M_{\text{ej}}/M_{\odot}) \leq -1$, taking the prior to an ejecta mass of $1 M_{\odot}$ was chosen for the purpose of upper limits that did not depend on the upper bound. For the lanthanide fraction, we will pin the values to $X_{\text{lan}} = [10^{-9}, 10^{-5}, 10^{-4}, 10^{-3}, 10^{-2}, 10^{-1}]$; note that for AT2017gfo, assuming the exact same model, a lanthanide fraction of $10^{-3.54}$ described the observational data best Coughlin et al. (2018).

3.1.2 Model II (Bulla 2019)

For the two-component models presented in Bulla (2019), each light curve depends on four parameters: the ejecta mass M_{ej} , the temperature at 1 d after the merger T_0 , the half-opening angle of the lanthanide-rich component Φ (with $\Phi = 0$ and $\Phi = 90^\circ$ corresponding to one-component lanthanide-free and lanthanide-rich models, respectively) and the observer viewing angle θ_{obs} (with $\cos \theta_{\text{obs}} = 0$ and $\cos \theta_{\text{obs}} = 1$ corresponding to a system viewed edge-on and face-on, respectively). Unlike Kasen et al. (2017), models by Bulla (2019) do not solve the full radiative transfer equation but rather simulate radiation transport for a given multidimensional ejecta morphology adopting parametrized opacities as input. The main advantage over Model I is the possibility to compute viewing-angle dependent observables for self-consistent multi-dimensional geometries in place of combining one-component models with different compositions and thus neglecting the interplay between different components. For this article, we compute light curves consistent with $-3 \leq \log_{10}(M_{\text{ej}}/M_{\odot}) \leq 0$, $15^\circ \leq \Phi \leq 30^\circ$, and $0 \leq \cos \theta_{\text{obs}} \leq 1$, while the temperature is fixed to the following values: $T_0 = [3000, 5000, 7000, 9000]$ K. Note that for AT2017gfo, $T_0 = 5000$ K, $\Phi = 30^\circ$, and $\cos \theta_{\text{obs}} = 0.9$ described the observational data best (Dhawan et al. 2019). Similar to the Kasen et al. (2017) model, the simulation set covers $-3 \leq \log_{10}(M_{\text{ej}}/M_{\odot}) \leq -1$, and we extend the prior to an ejecta mass of $1 M_{\odot}$.

3.1.3 Model III (Hotokezaka and Nakar 2019)

For the two-component models presented in Hotokezaka & Nakar (2019), the light curves are computed based on the Arnett analytic model (Arnett 1982) and a blackbody spectrum with a specific temperature at the photosphere. It assumes spherical ejecta of which the inner part is composed of high-opacity material and the outer part is composed of low-opacity material. In this model, thermalization of gamma-rays and electrons produced by each radioactive decay is taken into account according to their injection energy. Each light curve depends on M_{ej} , the ejecta velocity v_{ej} , the dividing velocity between the inner and outer part and the opacity of the two-components, κ_{low} and κ_{high} . The same prior range for the ejecta mass and velocity as in Model I is used. The model also depends on the lower and upper limits of the velocity distribution, which we set as free parameters within the range of $v_{\text{min}}/v_{\text{ej}} \in [0.1, 1.0]$ and $v_{\text{max}}/v_{\text{ej}} \in [1.0, 2.0]$.

3.1.4 Model-independent remarks

Models I, II, and III use similar nuclear heating rates ϵ_{nuc} , in units of ergs per second per gram. Model I assumes $\epsilon_{\text{nuc}} =$

$10^{10} t^{-1.3} \text{ erg g}^{-1} \text{ s}^{-1}$ where t is in days (Metzger et al. 2010). Model II, instead, adopts heating rates from Korobkin et al. (2012), $\epsilon_{\text{nuc}} = \epsilon_0 \left(\frac{1}{2} - \frac{1}{\pi} \arctan \frac{t-t_0}{\sigma} \right)^\alpha \left(\frac{\epsilon_{\text{th}}}{0.5} \right)$, with $\epsilon_0 = 2 \times 10^{18} \text{ erg g}^{-1} \text{ s}^{-1}$, $t_0 = 1.3 \text{ s}$, $\sigma = 0.11 \text{ s}$, $\alpha = 1.3$, and $\epsilon_{\text{th}} = 0.5$. In principle, Model III computes the radioactive power using the solar r-process abundance pattern with a minimum atomic mass number of 85. This is however computationally too expensive when sampling over many light curves, so in the analysis presented in Section 3.2 we fix the heating rate to the same as Model II. Although the previous formula provides a better description of nuclear heating rates at short time-scales, $t \lesssim 10 \text{ s}$, the agreement between the different rates is excellent at epochs of interest in this study, $t \gtrsim 1 \text{ d}$.

Within our analysis, we compare the light curves to one-sided Gaussian distributions, where we have taken the mean to be the upper limit from the telescope in the given passband and the mean distance from the gravitational-wave skymaps. We include a distance variation in our analysis by sampling over a changing ‘zero-point’ in the light curves consistent with the distance uncertainty stated in the GW alerts. This is computed by adding a distance modulus consistent with the distance variation from the localizations. While this approach does not account for the exact three-dimensional skymap, it provides representative constraints and limits.

Fig. 1 gives an example of this approach for the candidate S190510g using the model of Kasen et al. (2017). It shows the upper limits derived from the Dark Energy Camera in horizontal lines for the three photometric bands g , r , and z . The absolute magnitudes correspond to the mean of the gravitational-wave distance. We also plot an example light curve consistent with these constraints. These include the uncertainty in distance sampling. Histograms of the ejecta masses (and other quantities) are made based on these light curves, creating the distributions derived in the following analyses.

3.2 Ejecta mass limits

In this section, we provide ejecta mass constraints from comparing different light-curve models to observational upper limits for S190425z, S190426c, S190510g, S190901ap, and S190910h. Specifically, we compute ejecta mass constraints for different values of one key quantity for each model: the lanthanide fraction (Model I), the temperature (Model II), and the opacities (Model III). Constraints on the ejecta mass are controlled by the impact of these three different parameters on the predicted kilonova brightness and colour. Increasing the lanthanide fraction (X_{lan} , Model I) and opacities (κ_{low} and κ_{high} , Model III) shifts the escaping radiation to longer wavelengths and, thus, leads to the transition from a ‘blue’ to a ‘red’ kilonova. The impact of the temperature (Model II) on the brightness and colour depends on the epoch since merger. However, at phases when data are most constraining ($\lesssim 2 \text{ d}$) an increase in temperature results in a shift of the emitted radiation from redder to bluer wavelengths. In particular, moving temperature from 3000 to 9000 K produces increasingly fainter kilonovae in both optical and near-infrared bands at these epochs.

Because of the different colour predictions, telescopes observing in different regions of the spectrum are associated with different ejecta mass limits. For instance, optical telescopes are generally more constraining to ‘blue’ kilonovae that have low lanthanide fractions.

3.2.1 S190425z

The top row of Fig. 2 shows the ejecta mass constraints for S190425z based on observations from ZTF (left, Kasliwal et al. 2019a) and

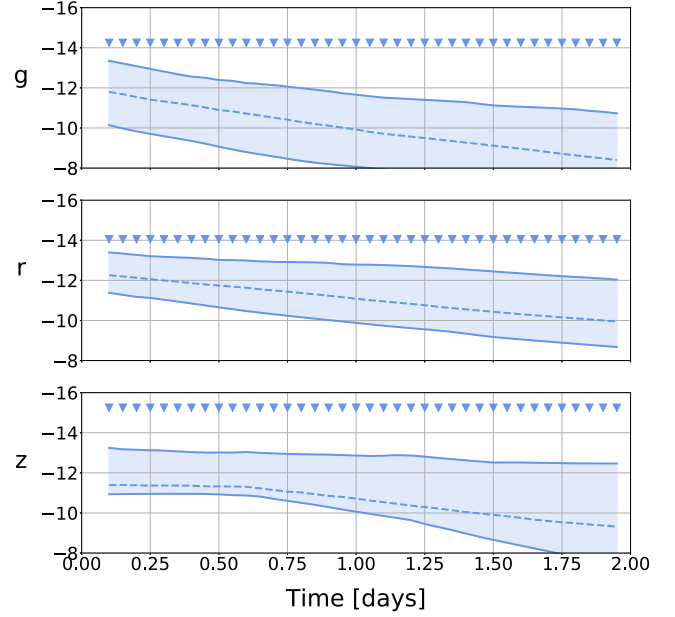


Figure 1. Variety of light curves consistent with the Dark Energy Camera based $g/r/z$ limits on S190510g (Andreoni et al. 2019b), where we show median and 90 per cent contours for light curves based on the Kasen et al. (2017) model.

PS1 (right, Smith et al. 2019). We mark the 90 per cent confidence with a horizontal dashed line. In general, the constraints on ejecta mass for the low lanthanide fractions are stronger than available for the ‘red kilonovae,’ which are hidden in the redder photometric bands, cf. Model I. This is a result of using optical telescopes, which cover a large percentage of the sky localization, but are generally more constraining to ‘blue’ kilonovae, i.e. those that have low lanthanide fractions. The i -band observations of PS1 lead to stronger constraints on the red side than is possible with ZTF for Model II, with similar constraints for Models I and III. With the higher intrinsic luminosities from Model II, the constraints in the redder bands from PS1 lead to notable improvements in the constraints. These constraints are not realized in Models I and III due to their lower intrinsic luminosities. We find that the different treatments of the heating rates and radiative transport yield significantly different ejecta mass constraints than imposed by the effective opacity, temperature, and lanthanide fraction differences, i.e. differences between the three models are larger than within the individual models. Most notably, Model II produces, across all considered temperature ranges, the most stringent constraints. Consequently, while Models I and III only disfavour (in the most optimistic scenarios) ejecta masses $M_{\text{ej}} \lesssim 0.1 M_{\odot}$, which is very hard to achieve for a BNS merger, Model II places upper bounds on the ejecta mass of $M_{\text{ej}} \lesssim 0.03 M_{\odot}$ for temperatures at or below 5000 K.

3.2.2 S190426c

The second row of Fig. 2 shows the ejecta mass constraints for S190426c based on the observations from ZTF (Kasliwal et al. 2019b) and the DECam (Goldstein et al. 2019b). Despite the smaller sky area requiring coverage and therefore generally deeper exposures, the larger distance to this object leads to limits that are worse than for the first event. However, for a number of parameter combinations, we find that ejecta masses above $\sim 0.1 M_{\odot}$ are ruled out based on the DECam observations. Furthermore, as for

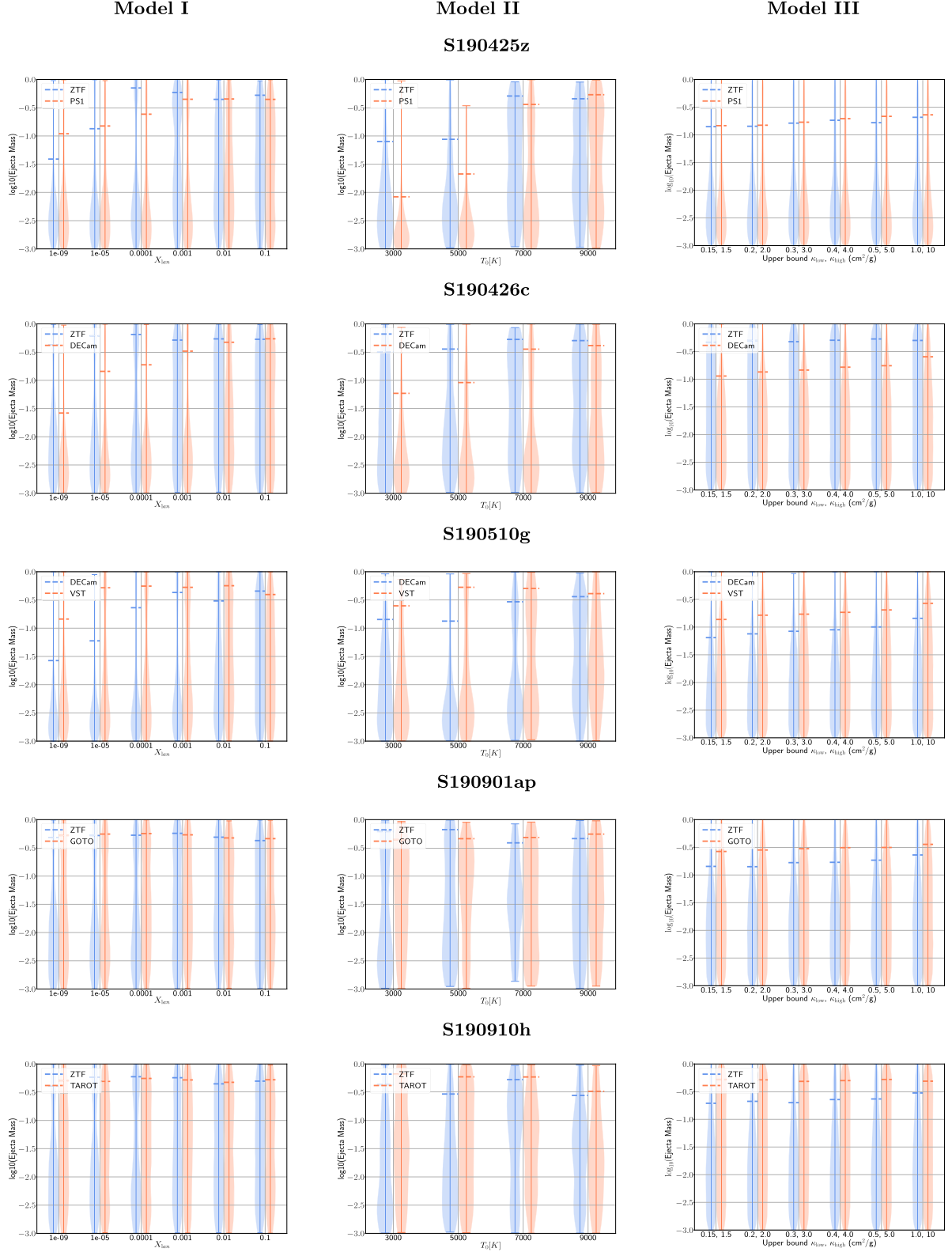


Figure 2. Probability density for the total ejecta mass for all considered events and all employed light-curve models. From the top down, the events are S190425z, S190426c, S190510g, S190901ap, and S190910h. From the left to the right, we show constraints as a function of lanthanide fraction for based on the Kasen et al. (2017) model, as a function of temperature for the Bulla (2019) model with $\Phi = 0^\circ$, and as a function of the opacity of the two components, κ_{low} and κ_{high} . For S190425z, we use the ZTF (left, Kasliwal et al. 2019a) and PS1 (right, Smith et al. 2019) limits. For S190426c, we use the ZTF (Kasliwal et al. 2019b) and the DECam (Goldstein et al. 2019b) limits. For S190510g, we use DECam (Andreoni et al. 2019b) and VST (Grado et al. 2019a). For S190901ap, we use the ZTF (Kool et al. 2019) and GOTO (Ackley et al. 2019b) observations. For S190910h, we use the ZTF (Stein et al. 2019a) and TAROT (Barynova et al. 2019b) observations.

S190425z, one obtains tighter constraints for blue kilonova (low lanthanide fractions and opacities) in Models I and III and for redder kilonovae in Model II.

3.2.3 S190510g

The third row of Fig. 2 shows the ejecta mass constraints for S190510g based on observations from DECam (Andreoni et al. 2019b) and VST (Grado et al. 2019a). The relative improvement of sensitivity between ZTF and DECam offsets the relative difference in distance estimates, yielding very similar ejecta mass constraints between the two BNS coalescence candidates, i.e. S190510g and S190425z. The inclusion of the three bands, g -, r -, and z -band observations, with DECam produces measurable constraints in both the blue and red bands; for example, with Model I, M_{ej} is $\lesssim 0.025 M_{\odot}$ for the lowest lanthanide fractions.

3.2.4 S190901ap

The fourth row of Fig. 2 shows the ejecta mass constraints for S190901ap based on observations from ZTF (Kool et al. 2019) and GOTO (Ackley et al. 2019b). Due to the large sky localization covering more than 10 000 deg², there was relatively minimal EM follow-up investigation. The larger distance to this potential BHNS system results in the shallowest constraints on ejecta mass for all considered candidates.

3.2.5 S190910h

The final row of Fig. 2 shows the ejecta mass constraints for S190910h based on observations from ZTF (Stein et al. 2019a) and TAROT (Barynova et al. 2019b). Due to the large sky localization covering more than 20 000 deg², there was relatively minimal EM follow-up investigation, and therefore, similar to the event above, there were essentially no constraints.

3.2.6 Summary

Considering the five individual constraints, we find that S190425z and S190426c provide overall the tightest constraints for a BNS and BHNS candidate, respectively. However, our analysis shows that even for these events, no constraints can be obtained with Model III or for Model I in case for ejecta with high lanthanide fractions. These loose constraints are mainly caused by the large distance to the individual candidate events, which are generally several times further away than GW170817. Considering the results obtained from Model II, we will describe in the next section how potential ejecta mass constraints lead to constraints on the binary properties of BNS and BHNS candidates. However, we want to emphasize that there are large systematic differences between the light-curve models and that the entire sky area provided by LIGO and Virgo has not been covered for all triggers. Thus, the following analysis should be rather interpreted as a proof of principle.

4 CONSTRAINING THE BINARY PARAMETERS

Within this section, we present as a proof of principle possible constraints for the binary properties of the BNS candidate S190425z and the BHNS candidate S190426c (under the assumption that the

source location was covered within the EM follow-up campaign). We focus on the results of Model II with a fixed temperature of 5000 K.⁴ This leads to a maximum total ejecta masses of $0.03 M_{\odot}$ for S190425z and $0.09 M_{\odot}$ for S190426c.

4.1 The BNS candidate S190425z

To ensure that the ejected material is massive enough to trigger a bright EM counterpart, the final remnant should not collapse promptly to a BH after the merger. As mentioned in the introduction, prompt collapse formation depends dominantly on the total mass of the binary. As shown in Bauswein et al. (2013), the total mass of the binary M has to be below a characteristic threshold mass:

$$M_{\text{thr}} = \left(2.380 - 3.606 \frac{M_{\text{TOV}}}{R_{1.6 M_{\odot}}} \right) M_{\text{TOV}} \quad (1)$$

with M_{TOV} being the maximum supported mass for a spherical NS and $R_{1.6 M_{\odot}}$ the radius of a $1.6 M_{\odot}$ NS. Recently, the threshold mass estimate was updated by Köppel et al. (2019) incorporating a non-linear dependence on the maximum allowed compactness and Agathos et al. (2019) derived a prompt-collapse threshold estimate based on new numerical relativity simulations, mainly publicly available at <http://www.computational-relativity.or> (Dietrich et al. 2018). For our rough estimates presented here, we will use, for simplicity, the criterion given in Bauswein et al. (2013).

While for close GW events it would be a valid assumption that all configurations without an EM counterpart have masses above the prompt threshold mass, $M > M_{\text{thr}}$, this assumption does not hold for systems with distances much larger than the one for GW170817, e.g. for S190425z. In general, the total ejecta mass, for which our previous analysis provided some upper limits, is related to the debris disc mass formed after the merger; here, we use the disc mass estimate presented in Coughlin et al. (2019b), where M_{disc} was a function on M/M_{thr} :

$$\log_{10} (m_{\text{disc}} [M_{\text{tot}}/M_{\text{thr}}]) = \max \left(-3, a \left(1 + b \tanh \left[\frac{c - M_{\text{tot}}/M_{\text{thr}}}{d} \right] \right) \right), \quad (2)$$

with the fitting parameters a, b, c, d (see Coughlin et al. 2019b). We emphasize that this estimate was based on a suite of numerical relativity simulations for equal-mass or near equal-mass systems, high mass ratio systems might lead to more massive discs (Kiuchi et al. 2019). The mass of the disc wind is then $M_{\text{wind}} = f M_{\text{disc}}$ with the unknown conversion factor f . This efficiency parameter remains very uncertain (Fernández et al. 2015; Siegel & Metzger 2018; Christie et al. 2019; Fernández et al. 2019) and we will vary it for our BNS analysis, $f \in [0.1, 0.4]$.⁵ Since a fraction of the ejecta will also be released dynamically during the merger, not all of the total ejecta comes from disc winds. As an indication, we present the disc wind estimate in Fig. 3 assuming 100 per cent of the total ejecta mass for S190425z are connected to the wind ejecta

⁴With the chosen temperature of 5000 K the predictions of Model II agree best with AT2017gfo (Dhawan et al. 2019). Thus, this temperature choice seems best suited for our analysis.

⁵Existing 3D simulations, which seed the accretion disc with a purely toroidal or purely poloidal magnetic field, fall at the high end of that interval, $f \sim [0.3-0.4]$. We conservatively allow for lower values of f to account for the possibility that about half of that ejecta is produced at early times, in magnetically driven winds that appear to depend on the strength and structure of the magnetic field and may still disappear for the small-scale turbulent magnetic fields that are most likely created in a NS merger.

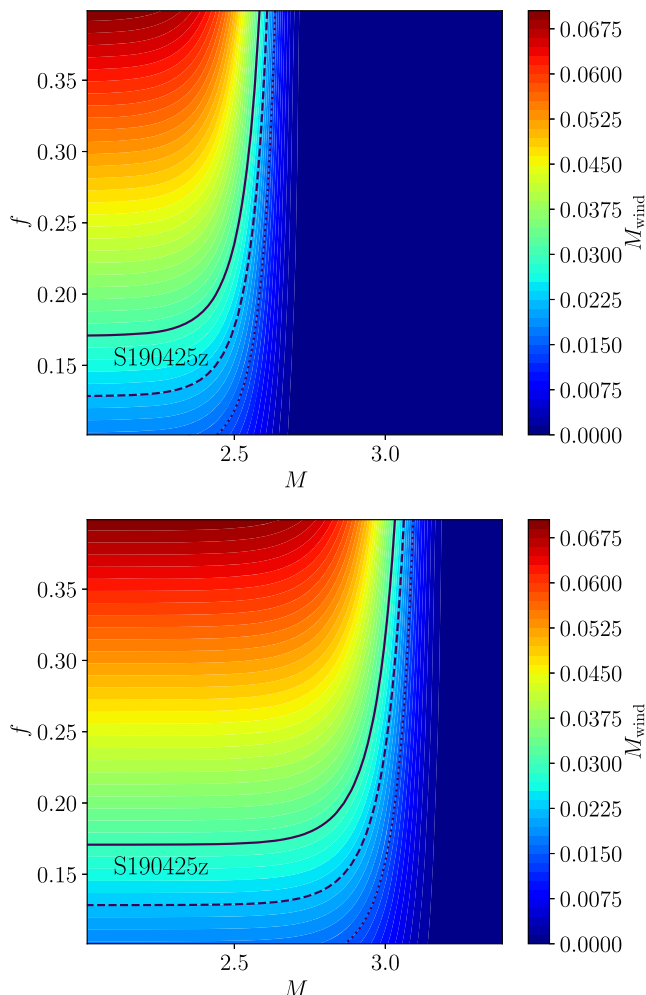


Figure 3. Disc wind ejecta as a function of the conversion factor f and the total mass of the binary M . We include the upper bounds from S190425z using Model II for 5000K assuming that the disc wind accounts for the entire ejecta mass (solid line), 75 per cent (dashed line) or for 50 per cent of the total ejecta (dotted line). The top panel assumes an EOS with a maximum TOV mass of $2.07 M_{\odot}$ and a radius of $R_{1.6 M_{\odot}} = 11.1$ km, while the bottom panel uses $M_{\text{TOV}} = 2.30 M_{\odot}$ and $R_{1.6 M_{\odot}} = 13.9$ km.

(solid black line), 75 per cent of the total mass is assigned to winds (dashed line), and half of the total ejecta comes from disc wind ejecta (dotted line).

The two panels in Fig. 3 refer to different choices of the maximum TOV-mass $2.07 M_{\odot}$ for the top and $2.30 M_{\odot}$ for the bottom panel. These values are motivated by the recent observation of J0740+6620 (Cromartie et al. 2019) and the upper bound on the maximum mass following from GW170817 (e.g. Margalit & Metzger 2017; Rezzolla et al. 2018; Shibata et al. 2019). In addition, we assume a radius $R_{1.6 M_{\odot}}$ of 11.1 km in the top and 13.9 km in the bottom panel, as derived in Coughlin et al. (2019b). These combinations of M_{TOV} and $R_{1.6 M_{\odot}}$ include the most extreme scenarios in terms of stiff and soft EOSs, and, thus, provide boundaries for our analysis. Considering the scenario for a very soft EOS, we find that the total mass of S190425z lies presumably above $2.40 M_{\odot}$ if the efficiency factor is about 20 per cent. Contrary for an efficiency factor of 20 per cent and a very stiff EOS, the total mass of S190425z would presumably be $2.9 M_{\odot}$.

4.2 The BHNS candidate S190426c

Similarly for BHNS systems, the absence of an observed kilonova constrains the initial parameters of the binary. As for the BNS case, the outflows from BHNS mergers can be divided into the dynamical ejecta, which is produced at the time of merger and typically lanthanide-rich (Deaton et al. 2013; Foucart et al. 2014; Kyutoku et al. 2018), and magnetically-driven or neutrino-driven disc winds produced in the 1–10 s following the merger, which have a more uncertain composition (Fernández et al. 2015; Just et al. 2015; Siegel & Metzger 2018; Fernández et al. 2019). The dynamical ejecta for NSs within the range of parameters used in numerical simulations so far is well modelled by the fit of Kawaguchi et al. (2016). Extrapolating that fit to more compact stars, however, leads to unphysical results (i.e. an increase in the ejected mass for more compact stars). Here, we use the modified formula

$$\frac{M_{\text{dyn}}}{M_{\text{NS}}^b} = \max \left(0, a_1 Q^{n_1} (1 - 2C_{\text{NS}}) - a_2 Q^{n_2} \frac{c^2 R_{\text{ISCO}}}{G M_{\text{BH}}} + a_3 \right) \quad (3)$$

with $Q = M_{\text{BH}}/M_{\text{NS}}$, M_{NS}^b is the baryon mass of the NS, $C_{\text{NS}} = GM_{\text{NS}}/(R_{\text{NS}}c^2)$ is its compactness, R_{ISCO} is the radius of the innermost stable circular orbit around the BH, and $a_1 = 0.007116$, $a_2 = 0.001436$, $a_3 = -0.0276$, $n_1 = 0.8636$, $n_2 = 1.6840$ (see Krüger et al., in preparation for a more detailed discussion). Note that R_{ISCO} is computed for circular orbits around a BH of dimensionless spin $\chi_{\text{eff}} = \chi_{\parallel}$, with χ_{\parallel} the component of the BH spin aligned with the orbital angular momentum of the binary. As a result, the ejected mass has a strong dependence in the aligned component of the BH spin. The total mass in the bound accretion disc surrounding the remnant BH can be estimated by subtracting M_{dyn} from the total amount of mass remaining outside of the BH after merger M_{out} . We compute M_{out} following the fit to numerical results provided in Foucart et al. (2018). Similarly to M_{dyn} , M_{out} depends on the mass ratio of the system, the compactness of the NS, and the aligned component of the BH spin. The mass in the disc winds is then $M_{\text{wind}} = f(M_{\text{out}} - M_{\text{dyn}})$. Since the BHNS case contains already a larger number of free parameters, we fix the conversion factor to $f \gtrsim 0.15$ (Fernández et al. 2015; Siegel & Metzger 2018; Fernández et al. 2019; Christie et al. 2019).

If S190426c was a BHNS merger within the region of the sky observed by ZTF and DECAM, and we assume the constraints obtained with Model II at 5000K, we argued that $M_{\text{ej}} = M_{\text{dyn}} + M_{\text{wind}}$ has to be less than $0.09 M_{\odot}$. Practically, this can be converted into a constraint excluding part of the 3-dimensional parameter space of $(Q, C_{\text{NS}}, \chi_{\parallel})$. Fig. 4 visualizes this constraint as a maximum allowed value for the component of the dimensionless BH spin aligned with the orbital angular momentum of the binary, as a function of NS size and binary mass ratio. We see that with this upper bound, the constraints on the parameter space of BHNS binaries are fairly weak: only large aligned BH spins combined with low-mass stars and relatively stiff equations of state can possibly be ruled out.

5 SUMMARY

We have presented an overview of the extensive searches for EM transients associated with a number of GW event triggers within the first half of the third observing run of Advanced LIGO and Advanced Virgo. Assuming that the individual sources were located in the covered sky region of the follow-up observations, we use three different kilonova models to derive possible upper limits on the ejecta mass compatible with the non-observation of EM signals

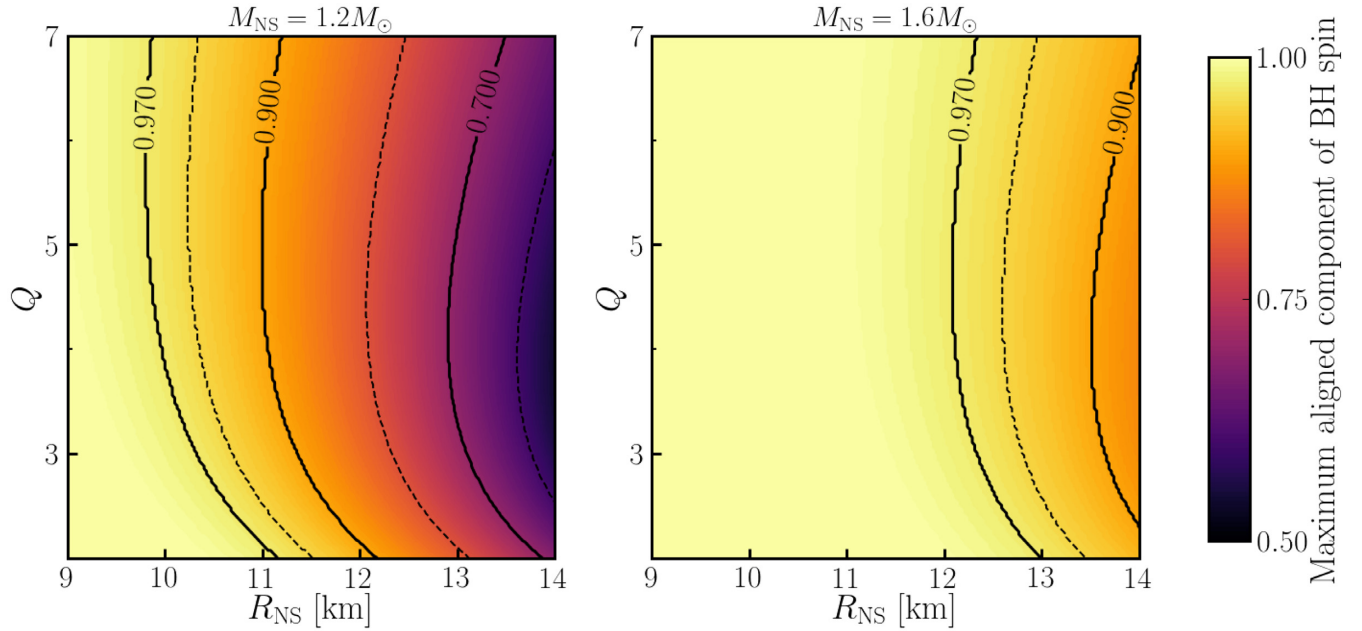


Figure 4. Maximum aligned component of the BH spin as a function of NS radius and binary mass ratio for S190426c, if that event was a BHNS merger within the region covered by follow-up observations. We show results for $M_{\text{NS}} = 1.2 M_{\odot}$ (left) and $M_{\text{NS}} = 1.6 M_{\odot}$, and require $M_{\text{ej}} < 0.09 M_{\odot}$ (Model II for 5000K). Dashed lines correspond to maximum spins of 0.6, 0.8, 0.95, and solid lines to maximum spins of 0.7, 0.9, 0.97. Only a small part of the parameter space (large aligned spin, low-mass NSs) can possibly be ruled out by observations. The constraints for more massive stars ($M_{\text{NS}} = 1.6 M_{\odot}$) are not reliable since the analytical models have not been tested for spins greater than ~ 0.9 .

for S190425z, S190426c, S190510g, S190901ap, and S190910h. Possibly informative constraints are obtained for S190425z and S190426c with the model of Bulla (2019). However, systematic uncertainties between different kilonova models are large and currently the dominating source of error in our analysis.

Based on our results, we computed potential lower limits on the total mass of S190425z from the non-existence of EM counterparts and find that it should have a total mass above $2.5 M_{\odot}$ if we assume a soft and $2.9 M_{\odot}$ if we assume a stiff EOS. Similarly, assuming that S190426c originated from a BHNS merger, we find that the non-observation of a kilonova could rule out large aligned BH spins combined with low-mass stars (for stiff EOSs).

Our simple analysis shows that even without direct GW information, beyond the provided skymap and classification probability, source properties can be constrained.⁶ More importantly, inverting our approach, one sees that a fast estimation of the total mass can potentially be used to classify if potential GW candidates will cause bright EM counterparts. A similar approach has been recently outlined in Margalit & Metzger (2019).

In general, the limits derived on the ejecta mass for the events in the first six months of O3 are not striking, which shows that one should be striving to take deeper observations, perhaps at the cost of a smaller sky coverage. Assuming that AT2017gfo is representative, ‘interesting’ limits are $\sim 0.05 M_{\odot}$, giving a ballpark limit to strive for. Those observations are most important at low latency, i.e. at times when kilonovae are brightest. In addition to adding and/or employing guiding to take longer observations, it might motivate the creation and use of stacking pipelines for survey facilities, for which this may be atypical.

⁶While we used *HasRemnant* to downselect the events, we did not rely on its results for the analysis.

ACKNOWLEDGEMENTS

Michael Coughlin is supported by the David and Ellen Lee Postdoctoral Fellowship at the California Institute of Technology. Tim Dietrich acknowledges support by the European Union’s Horizon 2020 research and innovation programme under grant agreement no. 749145, BNSmergers. Sarah Antier is supported by the CNES Postdoctoral Fellowship at Laboratoire Astroparticule et Cosmologie. MB acknowledges support from the G.R.E.A.T research environment funded by the Swedish National Science Foundation. Francois Foucart gratefully acknowledges support from NASA through grant no. 80NSSC18K0565 and from the NSF through grant no. PHY-1806278. The light-curve fitting/upper limits code used here is available at <https://github.com/mcoughlin/gwemlightcurves>.

REFERENCES

- Abbott B. P. et al., 2017, *Phys. Rev. Lett.*, 119, 161101
- Abbott B. P. et al., 2017a, *Nature*, 551, 85
- Abbott B. P. et al., 2017b, *ApJ*, 848, L12
- Abbott B. P. et al., 2017c, *ApJ*, 848, L13
- Abbott B. P. et al., 2019, *ApJ*, 875, 161
- Ackley K. et al., 2019a, *GCN Circ.*, 25337
- Ackley K. et al., 2019b, *GCN Circ.*, 25654
- Agathos M., Zappa F., Bernuzzi S., Perego A., Breschi M., Radice D., 2019, preprint ([arXiv:1908.05442](https://arxiv.org/abs/1908.05442))
- Anand S. et al., 2019, *GCN Circ.*, 25706
- Andreoni I. et al., 2019a, preprint ([arXiv:1910.13409](https://arxiv.org/abs/1910.13409))
- Andreoni I. et al., 2019b, *ApJ*, 881, L16
- Arcavi et al., 2017, *Nature*, 551, 64
- Arnett W. D., 1982, *ApJ*, 253, 785
- Baker T., Bellini E., Ferreira P. G., Lagos M., Noller J., Sawicki I., 2017, *Phys. Rev. Lett.*, 119, 251301
- Barynova K. et al., 2019a, *GCN Circ.*, 25666
- Barynova K. et al., 2019b, *GCN Circ.*, 25780

- Bauswein A., Baumgarte T. W., Janka H. T., 2013, *Phys. Rev. Lett.*, 111, 131101
- Bauswein A. et al., 2017, *ApJ*, 850, L34
- Bellm E. C. et al., 2018, *PASP*, 131, 018002
- Bhalerao V. et al., 2019, GCN Circ., 24258
- Blazek M. et al., 2019a, GCN Circ., 24227
- Blazek M. et al., 2019b, GCN Circ., 24327
- Bulla M., 2019, *MNRAS*, 489, 5037
- Capano C. D. et al., 2019, preprint ([arXiv:1908.10352](https://arxiv.org/abs/1908.10352))
- Christensen N. et al., 2019, GCN Circ., 25599
- Christie I. M., Lalakos A., Tchekhovskoy A., Fernández R., Foucart F., Quataert E., Kasen D., 2019, *MNRAS*, 490, 4811
- Cook D. O. et al., 2019, GCN Circ., 24232
- Coughlin M., Dietrich T., Kawaguchi K., Smartt S., Stubbs C., Ujevic M., 2017, *ApJ*, 849, 12
- Coughlin M. W. et al., 2018, *MNRAS*, 480, 3871
- Coughlin M. W., Dietrich T., Heinzel J., Khetan N., Antier S., Christensen N., Coulter D. A., Foley R. J., 2019a, preprint ([arXiv:1908.00889](https://arxiv.org/abs/1908.00889))
- Coughlin M. W., Dietrich T., Margalit B., Metzger B. D., 2019b, *MNRAS*, 489, L91
- Coughlin M. W. et al., 2019b, *ApJL*, 885, 1
- Coulter D. A. et al., 2017, *Science*, 358, 1556
- Creminelli P., Vernizzi F., 2017, *Phys. Rev. Lett.*, 119, 251302
- Cromartie H. T. et al., 2019, *Nat Astron*, in press
- Dado S., Dar A., 2019, preprint ([arXiv:1910.06163](https://arxiv.org/abs/1910.06163))
- De K. et al., 2019, GCN Circ., 24187
- Deaton M. B. et al., 2013, *ApJ*, 776, 47
- Dekany S. et al., 2019, *PASP*, submitted
- Dhawan S., Bulla M., Goobar A., Sagués Carracedo A., Setzer C. N., 2019, preprint ([arXiv:1909.13810](https://arxiv.org/abs/1909.13810))
- Dichiara S. et al., 2019, GCN Circ., 25352
- Dietrich T., Ujevic M., 2017, *Class. Quantum Gravity*, 34, 105014
- Dietrich T. et al., 2018, *Class. Quantum Gravity*, 35, 24LT01
- Doctor Z., Farr B., Holz D. E., Pürrer M., 2017, *Phys. Rev. D*, 96, 123011
- Eichler D., Livio M., Piran T., Schramm D. N., 1989, *Nature*, 340, 126
- Etienne Z. B., Liu Y. T., Shapiro S. L., Baumgarte T. W., 2009, *Phys. Rev. D*, 79, 044024
- Ezquiaga J. M., Zumalacárregui M., 2017, *Phys. Rev. Lett.*, 119, 251304
- Fernández R., Kasen D., Metzger B. D., Quataert E., 2015, *MNRAS*, 446, 750
- Fernández R., Tchekhovskoy A., Quataert E., Foucart F., Kasen D., 2019, *MNRAS*, 482, 3373
- Foucart F., 2012, *Phys. Rev. D*, 86, 124007
- Foucart F. et al., 2014, *Phys. Rev. D*, 90, 024026
- Foucart F., Hinderer T., Nissanke S., 2018, *Phys. Rev. D*, 98, 081501
- Goldstein D. A. et al., 2019a, *ApJ*, 881, L7
- Goldstein D. A. et al., 2019b, GCN Circ., 24257
- Grado A. et al., 2019a, GCN Circ., 24484
- Grado A. et al., 2019b, GCN Circ., 25371
- Graham M. J. et al., 2019, *PASP*, 131, 078001
- Groot P. et al., 2019, GCN Circ., 25340
- Hankins M. et al., 2019a, GCN Circ., 24284
- Hankins M. et al., 2019b, GCN Circ., 25358
- Hotokezaka K., Nakar E., 2019, preprint ([arXiv:1909.02581](https://arxiv.org/abs/1909.02581))
- Hotokezaka K., Kiuchi K., Kyutoku K., Okawa H., Sekiguchi Y.-i., Shibata M., Taniguchi K., 2013, *Phys. Rev. D*, 87, 024001
- Hotokezaka K., Nakar E., Gottlieb O., Nissanke S., Masuda K., Hallinan G., Mooley K. P., Deller A., 2019, *Nature Astron*, 3, 940
- Im M. et al., 2019, GCN Circ., 24466
- Just O., Bauswein A., Pulpillo R. A., Goriely S., Janka H. T., 2015, *MNRAS*, 448, 541
- Kapadia S. J. et al., 2019, preprint ([arXiv:1903.06881](https://arxiv.org/abs/1903.06881))
- Kasen D., Metzger B., Barnes J., Quataert E., Ramirez-Ruiz E., 2017, *Nature*, 551, 80
- Kasliwal M. M. et al., 2019a, GCN Circ., 24191
- Kasliwal M. M. et al., 2019b, GCN Circ., 24283
- Kawaguchi K., Kyutoku K., Shibata M., Tanaka M., 2016, *ApJ*, 825, 52
- Kilpatrick C. et al., 2019, GCN Circ., 25350
- Kim J. et al., 2019, GCN Circ., 25342
- Kiuchi K., Kyutoku K., Shibata M., Taniguchi K., 2019, *ApJ*, 876, L31
- Klotz A. et al., 2019, GCN Circ., 25338
- Kool E. et al., 2019, GCN Circ., 25616
- Köppel S., Bovard L., Rezzolla L., 2019, *ApJ*, 872, L16
- Korobkin O., Rosswog S., Arcones A., Winteler C., 2012, *MNRAS*, 426, 1940
- Kyutoku K., Ioka K., Okawa H., Shibata M., Taniguchi K., 2015, *Phys. Rev. D*, 92, 044028
- Kyutoku K., Kiuchi K., Sekiguchi Y., Shibata M., Taniguchi K., 2018, *Phys. Rev. D*, 97, 023009
- Lattimer J. M., Schramm D. N., 1974, *ApJ*, 192, L145
- Lattimer J. M., Schramm D. N., 1976, *ApJ*, 210, 549
- Lee W. H., Ramirez-Ruiz E., 2007, *New J. Phys.*, 9, 17
- Li B. et al., 2019, GCN Circ., 24465
- LIGO Scientific Collaboration, Virgo Collaboration, 2019a, GCN Circ., 24168
- LIGO Scientific Collaboration, Virgo Collaboration, 2019b, GCN Circ., 24228
- LIGO Scientific Collaboration, Virgo Collaboration, 2019c, GCN Circ., 24237
- LIGO Scientific Collaboration, Virgo Collaboration, 2019d, GCN Circ., 24279
- LIGO Scientific Collaboration, Virgo Collaboration, 2019e, GCN Circ., 24411
- LIGO Scientific Collaboration, Virgo Collaboration, 2019f, GCN Circ., 24442
- LIGO Scientific Collaboration, Virgo Collaboration, 2019g, GCN Circ., 24448
- LIGO Scientific Collaboration, Virgo Collaboration, 2019h, GCN Circ., 24489
- LIGO Scientific Collaboration, Virgo Collaboration, 2019i, GCN Circ., 24591
- LIGO Scientific Collaboration, Virgo Collaboration, 2019j, GCN Circ., 24656
- LIGO Scientific Collaboration, Virgo Collaboration, 2019k, GCN Circ., 25087
- LIGO Scientific Collaboration, Virgo Collaboration, 2019l, GCN Circ., 25187
- LIGO Scientific Collaboration, Virgo Collaboration, 2019m, GCN Circ., 25208
- LIGO Scientific Collaboration, Virgo Collaboration, 2019n, GCN Circ., 25296
- LIGO Scientific Collaboration, Virgo Collaboration, 2019o, GCN Circ., 25324
- LIGO Scientific Collaboration, Virgo Collaboration, 2019p, GCN Circ., 25333
- LIGO Scientific Collaboration, Virgo Collaboration, 2019q, GCN Circ., 25367
- LIGO Scientific Collaboration, Virgo Collaboration, 2019r, GCN Circ., 25442
- LIGO Scientific Collaboration, Virgo Collaboration, 2019s, GCN Circ., 25549
- LIGO Scientific Collaboration, Virgo Collaboration, 2019t, GCN Circ., 25606
- LIGO Scientific Collaboration, Virgo Collaboration, 2019u, GCN Circ., 25614
- LIGO Scientific Collaboration, Virgo Collaboration, 2019v, GCN Circ., 25695
- LIGO Scientific Collaboration, Virgo Collaboration, 2019w, GCN Circ., 25707
- LIGO Scientific Collaboration, Virgo Collaboration, 2019x, GCN Circ., 25723
- LIGO Scientific Collaboration, Virgo Collaboration, 2019y, GCN Circ., 25778
- LIGO Scientific Collaboration, Virgo Collaboration, 2019z, GCN Circ., 25814

- LIGO-Virgo Collaboration, 2019, GCN Circ., 25876
- Li L.-X., Paczynski B., 1998, *ApJ*, 507, L59
- Lipunov V. et al., 2017, *ApJ*, 850, L1
- Lipunov V. et al., 2019a, GCN Circ., 24167
- Lipunov V. et al., 2019b, GCN Circ., 24236
- Lipunov V. et al., 2019c, GCN Circ., 24436
- Lipunov V. et al., 2019d, GCN Circ., 25322
- Lipunov V. et al., 2019e, GCN Circ., 25609
- Lipunov V. et al., 2019f, GCN Circ., 25694
- Lipunov V. et al., 2019g, GCN Circ., 25712
- Lipunov V. et al., 2019h, GCN Circ., 25812
- Lundquist M. J. et al., 2019, *APJ*, 881, L26
- Margalit B., Metzger B. D., 2017, *ApJ*, 850, L19
- Margalit B., Metzger B. D., 2019, *ApJL*, 880, 1
- Masci F. J. et al., 2018, *PASP*, 131, 018003
- McBrien O. et al., 2019, GCN Circ., 24197
- Melandri A. et al., 2019, GCN Circ., 24340
- Metzger B. D. et al., 2010, *MNRAS*, 406, 2650
- Mochkovitch R., Hernanz M., Isern J., Martin X., 1993, *Nature*, 361, 236
- Mooley K. P. et al., 2017, *Nature*, 554, 207
- Nakar E., 2007, *Phys. Rept.*, 442, 166
- Narayan R., Paczynski B., Piran T., 1992, *ApJ*, 395, L83
- Niino Y. et al., 2019, GCN Circ., 24299
- Noysena K. et al., 2019, GCN Circ., 25749
- Paczynski B., 1991, *AcA*, 41, 257
- Pannarale F., Tonita A., Rezzolla L., 2011, *ApJ*, 727, 95
- Pedregosa F. et al., 2011, *J. Mach. Learn. Res.*, 12, 2825
- Pereyra E. et al., 2019, GCN Circ., 25737
- Radice D., Dai L., 2019, *Eur. Phys. J.*, A55, 50
- Radice D., Perego A., Zappa F., Bernuzzi S., 2018, *ApJ*, 852, L29
- Rasmussen C. E., Williams C. K. I., 2006, *Gaussian Processes for Machine Learning*. MIT Press, Cambridge, MA, USA
- Rezzolla L., Most E. R., Weih L. R., 2018, *ApJ*, 852, L25
- Roberts L. F., Kasen D., Lee W. H., Ramirez-Ruiz E., 2011, *ApJ*, 736, L21
- Sakstein J., Jain B., 2017, *Phys. Rev. Lett.*, 119, 251303
- Sari R., Piran T., Narayan R., 1998, *ApJ*, 497, L17
- Savchenko V. et al., 2017, *ApJ*, 848, L15
- Shappee B. et al., 2019, GCN Circ., 24309
- Shibata M., Zhou E., Kiuchi K., Fujibayashi S., 2019
- Siegel D. M., Metzger B. D., 2018, *ApJ*, 858, 52
- Singer et al., 2019, GCN Circ., 25343
- Smartt S. et al., 2019a, GCN Circ., 24517
- Smartt S. et al., 2019b, GCN Circ., 25922
- Smith K. W. et al., 2019, GCN Circ., 24210
- Soares-Santos M. et al., 2017, *ApJ*, 848, L16
- Soares-Santos M. et al., 2019, GCN Circ., 25336
- Srivastav S. et al., 2019, GCN Circ., 25375
- Steehgs D. et al., 2019a, GCN Circ., 24224
- Steehgs D. et al., 2019b, GCN Circ., 24291
- Stein R. et al., 2019a, GCN Circ., 25722
- Stein R. et al., 2019b, GCN Circ., 25899
- Tanvir N. R., Levan A. J., Fruchter A. S., Hjorth J., Hounsell R. A., Wiersema K., Tunnicliffe R. L., 2013, *Nature*, 500, 547
- Troja E. et al., 2017, *Nature*, 551, 71
- Turpin D. et al., 2019, GCN Circ., 25847
- Valenti S. et al., 2017, *ApJ*, 848, L24
- Veitch J. et al., 2015, *Phys. Rev. D*, 91, 042003
- Watson A. M. et al., 2019, GCN Circ., 24310
- Wei J. et al., 2019, GCN Circ., 25648
- Xu D. et al., 2019a, GCN Circ., 24190
- Xu D. et al., 2019b, GCN Circ., 24285
- Xu D. et al., 2019c, GCN Circ., 24286
- Xu D. et al., 2019d, GCN Circ., 24476
- Yoshida M. et al., 2019, GCN Circ., 24450
- Zhu Z. et al., 2019, GCN Circ., 24475

APPENDIX

See Tables A1 and A2.

Table A1. Reports of the observations by various teams of the sky localization area of gravitational-wave alerts of the possible BNS candidates S190425z, S190510g, S190901ap, S190910h, and S190930t. Teams that employed ‘galaxy targeting’ during their follow-up are not mentioned here. In the case where numbers were not reported or provided upon request, we recomputed some of them; if this was not possible, we add —.

Telescope	Filter	Limit (mag)	Delay aft. GW (h)	Duration (h)	GW sky localization area Name	Coverage (per cent)	Ref.
S190425z							
ATLAS	<i>o</i> band	19.5	0.8	6.2	bayestar ini	37	McBrien et al. (2019)
CNEOST	Clear	≈20	27.5	4.8	bayestar ini	10	Xu et al. (2019b)
GOTO	<i>L</i> band	20.5	11.7	8.9	bayestar ini	30	Steeeghs et al. (2019a)
GRANDMA-TAROT	Clear	17.5	6.7	<63	LALInference	3	Blazek et al. (2019a)
GROWTH-Gattini-IR	<i>J</i> band	15.5	1.0	27.8	LALInference	19	De et al. (2019)
MASTER-network	Clear	≈18.5	≈0.0	144	bayestar ini	37	Lipunov et al. (2019a)
Pan-STARRS	<i>i</i> band	21.5	1.3	<19	bayestar ini	28	Smith et al. (2019)
SAGUARO	<i>g</i> band	≈21	1.3	1.3	bayestar ini	3	Lundquist et al. (2019)
Xinglong-Schmidt	Clear	18	4.5	0.9	bayestar ini	3	Xu et al. (2019a)
Zwicky Transient Facility	<i>g/r</i> band	≈21	1.0	27.8	LALInference	21	Kasliwal et al. (2019a)
S190510g							
ATLAS	<i>o</i> band	19.5	4.2	<12	LALInference	4	Smartt et al. (2019a)
CNEOST	Clear	≈18.5	9.9	3.3	bayestar ini	13	Li et al. (2019)
Dabancheng/HMT	Clear	≈18	13.0	6.0	bayestar ini	≈8	Xu et al. (2019d)
GRAWITA-VST	<i>r</i> sloan	22	21.1	<6	LALInference	50	Grado et al. (2019a)
GROWTH-DECAM	<i>g/r/z</i> band	21.7/22.3/21.2	3.0	18.5	LALInference	65	Andreoni et al. (2019b)
HSC	<i>Y</i> band	22.7	<6	<12	bayestar ini	12	Yoshida et al. (2019)
KMTNet	<i>R</i> band	21.7	13.6	<12	LALInference	66	Im et al. (2019)
MASTER-network	Clear	≈18.5	≈0	144	bayestar ini	52	Lipunov et al. (2019c)
Pan-STARRS	<i>w/i</i> band	20.5	4.2	<12	LALInference	4	Smartt et al. (2019a)
Xinglong-Schmidt	Clear	18.5	9.8	5.8	bayestar ini	19	Zhu et al. (2019)
DECAM-KMTNet	<i>r-R</i> band	>22	3.0	<24	LALInference	69	—
CNEOST-HMT-MASTER-	Clear	>18	1.0	<24	LALInference	71	—
Xinglong-TAROT							
S190901ap							
GOTO	<i>L</i> band	20	0.1	54	bayestar ini	28	Ackley et al. (2019b)
GRANDMA-TAROT	Clear	17.5	0.4	<58.6	LALInference	9	Barynova et al. (2019a)
MASTER-network	Clear	≈18.5	5.5	168	bayestar ini	32	Lipunov et al. (2019e)
SVOM-GWAC	<i>R</i> band	16.3	12.0	9	bayestar ini	16	Wei et al. (2019)
Zwicky Transient Facility	<i>g/r</i> band	20.7/20.7	3.6	~72	LALInference	73	Kool et al. (2019)
S190910h							
GRANDMA-TAROT	Clear	18	10.5	<129	LALInference	1	Barynova et al. (2019b)
MASTER-network	Clear	≈18.5	2.6	144	bayestar ini	8	Lipunov et al. (2019g)
Zwicky Transient Facility	<i>g/r</i> band	20.7/20.7	1.80	1.5	bayestar ini	34	Stein et al. (2019a)
S190930t							
ATLAS	<i>o</i> band	19.5	0.0	144	bayestar ini	19	Smartt et al. (2019b)
MASTER-network	Clear	≈18.5	≈0	72	bayestar ini	10	Lipunov et al. (2019g)
Zwicky Transient Facility	<i>g/r</i> band	20.4/20.4	11.9	10.0	bayestar ini	45	Stein et al. (2019b)

Table A2. Reports of the observations by various teams of the sky localization area of gravitational-wave alerts of possible BHNS candidates S190426c, S190814bv, S190910d, and S190923y. Teams that employed ‘galaxy targeting’ during their follow-up are not mentioned here. In the case where numbers were not reported or provided upon request, we recomputed some of them; if this was not possible, we add —.

Telescope	Filter	Limit (mag)	Delay aft. GW (h)	Duration (h)	GW sky localization area name	coverage (per cent)	Reference
S190426c							
ASAS-SN	<i>g</i> band	≈18	—	≈24	bayestar ini	86	Shappee et al. (2019)
CNEOST	Clear	≈20	1.3	3.5	bayestar ini	35	Xu et al. (2019c)
DDOTI/OAN	<i>w</i> band	≈18.5	14.7	4.9	bayestar ini	≈37	Watson et al. (2019)
GOTO	<i>g</i> band	19.9	5.3	8.9	LALInference	54	Steehhs et al. (2019b)
GRANDMA-OAJ	<i>r</i> band	19.6	6.3	4.9	bayestar ini	11	Blazek et al. (2019b)
GRAWITA-Asiago	<i>r</i> band	≈16	6.9	0.5	LALInference	2	Melandri et al. (2019)
GROWTH-DECAM	<i>r/z</i> band	22.9/22.5	7.6	11.5	LALInference	8.0	Goldstein et al. (2019a)
GROWTH-Gattini-IR	<i>J</i> band	≈14.5	11.8	9.8	bayestar ini	92	Hankins et al. (2019a)
GROWTH-INDIA	<i>r</i> band	20.5	2.0	29.4	bayestar ini	4	Bhalerao et al. (2019)
J-GEM	Clear	20	19	—	bayestar ini	—	Niino et al. (2019)
MASTER-network	Clear	≈18.5	≈0	144	bayestar ini	53	Lipunov et al. (2019b)
SAGUARO	<i>g</i> band	≈21	41.8	≈24	bayestar ini	5	Lundquist et al. (2019)
Zwicky Transient Facility	<i>g/r</i> band	≈21	13.0	31.3	bayestar ini	75	Kasliwal et al. (2019b)
S190814bv							
ATLAS	<i>o</i> band	>16	<12	24.0	LALInference	99	Srivastav et al. (2019)
DESGW-DECam	<i>r/i</i> band	23.4,22.6	9.5	≈96	LALInference	90	Soares-Santos et al. (2019)
DDOTI/OAN	<i>w</i> band	≈18.5	10.8	3.9	LALInference	90	Dichiara et al. (2019)
GOTO	<i>L</i> band	18.4	3.5	5.0	LALInference	83	Ackley et al. (2019a)
GRAWITA-VST	<i>r</i> sloan	≈22	11.7	1.3	LALInference	65	Grado et al. (2019b)
GROWTH-Gattini-IR	<i>J</i> band	≈17.0	8.9	96.0	bayestar ini	90	Hankins et al. (2019b)
KMTNet	<i>R</i> band	22.0	8.4	<12	LALInference	98	Kim et al. (2019)
MASTER-network	Clear	≈18	0.4	6.7	bayestar ini	98	Lipunov et al. (2019d)
MeerLICHT	<i>u/q/i</i> band	18.5/19.7/19.1	2.0	5.1	bayestar HLV	95	Groot et al. (2019)
Pan-STARRS	<i>i/z</i> band	20.8/20.3	15.5	2.55	LALInference	89	Smartt et al. (2019a)
Swope	<i>r</i> band	≈20.0	6.3	5.1	LALInference	42	Kilpatrick et al. (2019)
GRANDMA-TCA	Clear	18.0	3.0	2.5	bayestar HLV	27	Klotz et al. (2019)
GRANDMA-TRE	Clear	17.0	0.5	1.0	LALInference	76	Christensen et al. (2019)
Zwicky Transient Facility	<i>g/r/i</i> band	20.3	13.3	1.7	bayestar ini HLV	86	Singer et al. (2019)
MASTER-TAROT	Clear	>17	0.5	<3	LALInference	89	—
S190910d							
DDOTI/OAN	<i>w</i> band	≈18.5	3.0	4.7	LALInference	5	Pereyra et al. (2019)
GRANDMA-TAROT	Clear	≈17.5	1.0	<67	LALInference	37	Noysena et al. (2019)
MASTER-network	Clear	≈18.5	≈0	144	bayestar ini	25	Lipunov et al. (2019f)
Zwicky Transient Facility	<i>g/r</i> band	20.8	1.5	1.5	bayestar ini	34	Anand et al. (2019)
S190923y							
GRANDMA-TAROT	Clear	≈17.5	3.7	<56.1	bayestar ini	26	Turpin et al. (2019)
MASTER-network	Clear	≈18.5	≈0	144	bayestar ini	58	Lipunov et al. (2019h)

This paper has been typeset from a \LaTeX file prepared by the author.